Limits of hydrogen analysis by atom probe tomography targeting Zr(Fe,Cr)<inf>2</inf> second phase particles in Zr-based fuel cladding

Journal of Nuclear Materials 601 (2024) 155343

Contents lists available at ScienceDirect

Journal of Nuclear Materials

journal homepage: www.elsevier.com/locate/jnucmat

Limits of hydrogen analysis by atom probe tomography targeting $Zr(Fe,Cr)_2$ second phase particles in Zr-based fuel cladding from reactor operation

David Mayweg [a,*], Johan Eriksson [a,b], Mohammad Sattari [a], Mattias Thuvander [a]

[a] Department of Physics, Chalmers University of Technology, Göteborg SE-412 96, Sweden
[b] Department of Chemistry and Chemical Engineering, Chalmers University of Technology, Göteborg SE-412 96, Sweden

GRAPHICAL ABSTRACT

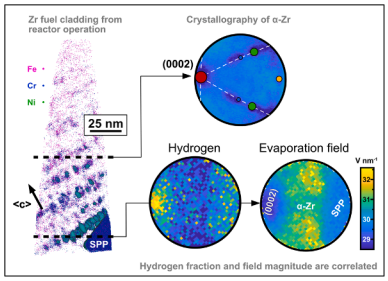

ARTICLE INFO

Keywords:
Atom probe tomography
Hydrogen analysis
Zircaloy
Second phase particles
Cryogenic-FIB
Field ion microscopy

ABSTRACT

We report results from atom probe tomography (APT) experiments capturing $Zr(Fe,Cr)_2$ second phase particles (SPPs) in Zircaloy-2-type fuel cladding after reactor operation. In light of recent reports of H trapping around SPPs, we assess the feasibility of H analysis in modern commercial atom probe instruments on this system. To this end we employed voltage and laser pulsing APT on specimens prepared by focused ion beam (FIB) at room and cryogenic temperature. Room temperature FIB caused transformation of the α-Zr matrix into δ-hydride, but left SPPs mostly unaffected. This indicates that α-Zr has a higher affinity for H than SPPs. However, even under optimized conditions, we were not able to find evidence for H trapping near SPPs located within the α-Zr matrix in cryogenically FIB sharpened specimens, where no hydride transformation occurs.

1. Introduction

Hydrogen pick-up (HPU) and associated hydride formation is one of the most relevant degradation mechanisms in Zr-based nuclear fuel claddings [1], which are standard in water-cooled and -moderated nuclear power reactors. Zr is used because of its small capture cross section for thermal neutrons and good corrosion resistance and these alloys contain typically > 98 wt% Zr. While most newly developed Zr-based claddings contain Nb (which are used in pressurized water reactors (PWRs)), the present work deals with *Zircaloy-2*-type cladding material – the main alloying elements are Sn, Fe, Cr, and Ni – as these alloys are still used in boiling water reactors (BWRs), and general insights regarding HPU and hydride formation would be relevant for all Zr-based materials. In *Zircaloy-2,* Sn is (at least initially) in solid solution while Fe, Cr, and Ni with a solubility of <10 ppm [2] form intermetallic precipitates $Zr(Fe,Cr)_2$ and $Zr_2(Fe,Ni)$ [3] that are often referred to as *second phase*

* Corresponding author.
E-mail addresses: david.mayweg@chalmers.se, david.mayweg@gmail.com (D. Mayweg).

https://doi.org/10.1016/j.jnucmat.2024.155343
Received 15 May 2024; Received in revised form 6 August 2024; Accepted 9 August 2024
Available online 11 August 2024

precipitates/particles (SPPs). In order to understand the processes of HPU and hydride precipitation it is of interest to find out which microstructural features are H sinks. Simulations have proposed that the α-Zr matrix in direct vicinity $Zr(Fe,Cr)_2$ precipitates are low-energy sites for H [4,5], a claim recently backed up by secondary ion mass spectrometry (SIMS) experiments on autoclave-corroded *Zircaloy-2* and *Zircaloy-4* spiked with deuterium (elemental symbol D or ^2H) [5].

However, virtually all experiments attempting to detect and especially quantify H are challenging tasks. Such is all the more true when it is attempted with the spatial resolution that is necessary to target SPPs that have diameters in the range of some ten to a few hundred nm prior to irradiation [6]. During irradiation, $Zr(Fe,Cr)_2$ SPPs are amorphized and dissolved, releasing Fe and Cr into the matrix [7–10]. This dissolution is promoted through irradiation damage from fast neutrons that create characteristic defects in hexagonal metals such as Zr. Such are a-loops on near-prismatic planes that align in layers parallel to basal planes and form early during irradiation as well as – much larger – c-loops that lie on basal planes and only emerge at higher fluence [11,12]. When Fe and Cr are redistributed during irradiation, they segregate to irradiation-induced defects (mostly at a-loops) [8,9].

Atom probe tomography (APT) is a technique that is capable of characterizing chemical compositions with a spatial resolution below 1 nm in 3D [13], while it can detect any element including – in principle – H. At the same time is has been pointed out by many authors that H quantification in APT is not straightforward, neither in general [14–16] nor for Zr [17,18]. The key challenge is to distinguish between H (species) originating from within the sample and contaminant H that appears to be nearly always present inside stainless-steel analysis chambers of commercial atom probe instruments [19] and is also picked up during specimen preparation [20]. Furthermore, the parameters used for specimen preparation, especially focused ion beam (FIB) milling and the APT experiment itself, play a significant role in the measured amount and distribution of detected H. One key challenge is that FIB-based preparation of thin specimens for APT and transmission electron microscopy (TEM) at ambient temperatures almost always leads to H ingress that causes transformation of α-Zr to δ-hydride [21–23] (sometimes also γ-hydride [21]). This H uptake and the subsequent transformation can be suppressed by performing the FIB preparation at cryogenic temperatures [21,24]. In the present work we report APT results of H measurements of specimens from irradiated fuel cladding that captured SPPs and discuss the influence of experimental set-ups and the limits of insights that can be gained from such experiments.

2. Materials and methods

We received segments of fuel cladding tubes from two from two alloys (further results have been published in [2,23,25]). The fuel rods with these tubes were located directly next to each other in a fuel assembly produced by *Westinghouse Electric Sweden AB* (Västerås, Sweden) and were removed after 2082 days of operation at 286 °C coolant temperature in the BWR Oskarshamn 3, operated by *OKG AB*, in 2008 and stored in a spent fuel pool (water temperature < 60 °C). They were then transported to *Studsvik Nuclear AB* (Nyköping, Sweden) in 2018 and, after de-fueling and cutting, delivered to *Chalmers University of Technology* (Gothenburg, Sweden) in 2019. The compositions in the as-produced condition are provided in Table 1. From each alloy, samples with damage levels of 9 and 19 dpa were investigated (in [2,23] we reported 8.6 and 38 dpa; we have since received the new value for the higher fluence samples after a reassessment from the manufacturer). There was no discernable difference between samples of equal damage level from the two alloys that could be observed by APT (e.g., the average matrix contents of Fe, Cr and Ni that we reported in [2] are only minutely different). In the following we do only identify the specimens with respect to their parent sample, but do not discuss alloys and damage levels separately. The bulk H concentration after operation (measured by hot vacuum extraction) was 200 ± 29 wt ppm (~ 1.8 at%) in the *Zircaloy-2* tube and 134 ± 9 wt ppm (~ 1.2 at%) in the *Zircaloy-2 Fe+* tube, respectively, most of which was present in hydrides. The model alloy *Zircaloy-2 Fe+* is similar to HiFi [26] with only a minor difference in Cr content.

Standard procedures for APT specimen preparation [27] were performed as follows: lift-out and mounting on Si coupons for APT and grids for correlative TEM and APT was carried out using an *FEI Versa 3D*, which was also used for annular milling at room temperature (RT). Annular FIB milling at RT in our materials virtually always leads to a transformation from α-Zr → δ-hydride [23]. It should be noted that *Ziracloy-4* and Nb-containing Zr alloys might be slightly less prone to this effect than the here investigated *Zircaloy-2*-type alloys. We additionally performed annular milling under cryogenic conditions on some specimens in a *Tescan GAIA3* equipped with a *Leica VCT-500* cryo-stage cooled with liquid N_2 (stage temperature below – 150 °C, cold trap below – 180 °C) to prevent H uptake [21,23,28]. This suppressed the transformation but resulted in a very low success rate in voltage pulsing mode and most specimens fractured after only a few hundred thousand ions had been detected. Specimen preparation for TEM was also performed under cryogenic conditions to suppress hydridation. After initial TEM imaging we attempted the removal of surface damage to improve the image quality in a *Fischione 1010* ion mill at – 96 °C. This, however, led to formation of hydrides on the foil's surface that prevented us from obtaining images of dislocation loops with better quality. These induced surface hydrides were different from FIB-induced hydrides, which penetrate through the bulk of the lamellae.

APT experiments were performed in a *LEAP 3000X HR* and a *LEAP 6000 XR* in voltage and laser pulsing mode; some experimental parameters are listed in Table 2. More detailed information and mass spectra of all datasets presented here can be found in the supplementary material. Field ion microscopy (FIM) was carried out in the *LEAP 3000X HR* at 17 K (minimum temperature, stage heater turned off) using Ne as imaging gas after evaporation of approximately 200,000 ions to clean the surface. This experiment was carried out using the software packages *LCC* and *DAVis*, and images were created from screenshots of eFIM videos. eFIM means that the multi-channel plate detector is used for recording FIM images as opposed to the classically employed fluorescent screen. Reconstructions (voxel size 1×1×1 nm, delocalization 1.5×3×3 nm) were created in *AP Suite 6.3* using the positions of crystallographic poles and interplanar spacings for calibration in the case of voltage pulsing APT experiments [29,30], whereas laser pulsing measurements were reconstructed with default parameters. Field evaporation images (FEIs) used for obtaining information about the crystallographic orientation of the specimens were created using *MATLAB* scripts from Breen et al. [31] and Heller et al. [32]. The field strengths were calculated using charge state ratios (CSRs) based on Kingham's theory [33] using the equation and parameters given by Tegg et al. [34]. The supplementary material

Table 1
Composition of cladding tubes in as-produced condition.

Alloy		Fe	Cr	Ni	Sn	O		C	Si	N	Al
Zircaloy-2 Fe+	(at%/at ppm)	0.58	0.31	0.097	1.00	0.68	/	900	290	250	<100
	(wt%/at ppm)	0.36	0.18	0.063	1.31	0.12	/	120	90	38	<30
Zircaloy-2	(at%/at ppm)	0.29	0.23	0.094	1.14	0.68	/	1100	290	260	<100
	(wt%/at ppm)	0.18	0.13	0.061	1.49	0.12	/	143	91	40	<30

Table 2
Overview of experimental parameters used in the APT measurements.

Data set shown in	Pulsing mode	Temperature (K)	Pulse fraction (%)	Laser pulse energy (LPE) (pJ)	Pulse frequency (kHz)	Detection rate (%)	LEAP model	Annular milling temperature (°C)
Figs. 2, 3	Voltage	92	20	–	250	0.2	3000X HR	< – 150
Fig. 4	Voltage	84	20	–	250	0.2	3000X HR	< – 150
Fig. 5	Voltage	70	20	–	200	0.2	6000 XR	ambient
Fig. 6	Laser	60	–	50	200	0.5	6000 XR	< – 150
Fig. 7	Laser	50	–	50	100, 200	0.5	6000 XR	ambient

includes the mass-to-charge spectra of the datasets presented in this paper as well as a spreadsheet containing more information about the experimental parameters used in the APT experiments. TEM was performed using an *FEI Titan 80–300* at 300 kV.

3. Results

3.1. TEM

Fig. 1(a) is a bright field image of a $Zr(Fe,Cr)_2$-SPP with near two-beam imaging conditions highlighting a-loops. The lamella is relatively thick so individual a-loops cannot be distinguished. The linear features near the SPP are therefore most likely arrays of a-loops potentially with significant segregation of Cr (as shown in many instances in the literature [7–10,23,35] and in the APT results in the following sections). Fig. 1(b) is a centered dark field image of the same SPP, the amorphous nature of which is demonstrated by the diffraction pattern shown in Fig. 1(c). This amorphous nature might extend to the Cr-rich clusters (or precipitates) that form when Cr released from SPPs segregates to a-loops. The damage level is such that most likely Fe has largely moved to the matrix, where it is located in clusters at a-loops, while most Cr is retained in the SPPs [36].

3.2. Voltage pulsing APT and FIM

Fig. 2 shows a reconstruction from a specimen sharpened under cryogenic conditions (*Zircaloy-2 Fe+,* 19 dpa). The measurement was performed in voltage pulsing mode with 20% pulse fraction (PF) at ~ 92 K, a pulse frequency of 250 kHz and a detection rate of 0.2%. We used this uncommonly high base temperature after approximately 20 measurements on specimens at 70 K had not resulted in a single dataset with more than a few 100,000 ions. While this is a comparatively high temperature where surface migration is expected [37,38], the field was still sufficiently high to avoid the presence of H_2^+ and H_3^+ [14,39,40], which makes interpretation of mass spectra relatively straightforward. Our measurement captured a part of a $Zr(Fe,Cr)_2$-SPP and Cr-rich clusters that are arranged in layers parallel to basal planes, thus resembling a-loop distributions found in irradiated Zr-alloys (see Fig. 2(a)). The FEI in Fig. 2(b) reveals the positions of several poles, which are labelled in the stereographic projection below. The fraction of H detected in α-Zr, including clusters and away from the main pole, is ~ 0.4 at%, while the SPP volume contains ~ 1.5 at% H. Here, H was detected mostly as H^+, but also some ZrH^{++} [41].

In addition to the Cr, Fe, and H profiles, the proximity histogram ([42], also called '*proxigram*') in Fig. 2(c) shows the Zr CSR (defined as the ratio of Zr^{+++} and Zr^{++} ions), which gives an indication of the electric field strength [33]. Simply put, higher field strengths lead to higher post-ionization of a field-evaporated ion and the detected charge states can in turn be used to estimate the field. This can be done globally for an entire mass spectrum to be used as an input for the reconstruction algorithm and it can be used to map field variations across a specimen (compare, e.g., [28]). The H-profile in Fig. 2(c) qualitatively follows the inverse of the CSR, i.e., H is low in the high-field region (~ 31.3 V/nm) and high in the low-field region (~ 29.8 V/nm).

Fig. 3 comprises additional information about the H distribution obtained from the last 400,000 ions of the α-Zr dataset seen in Fig. 2. Fig. 3(a) displays the single hit ions and highlight density variations. The position of the (0002) pole in the upper left is visible and the inset shows

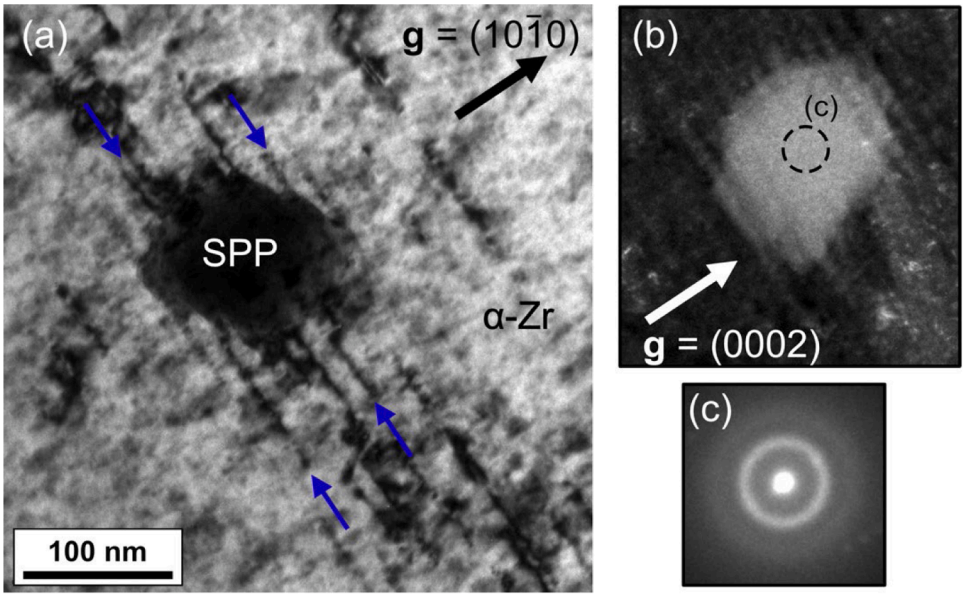

Fig. 1. TEM of an amorphized $Zr(Fe,Cr)_2$-SPP in *Zircaloy-2 Fe+* (19 dpa): (a) Bright field image, zone axis close to $[\bar{1}2\bar{1}6]$, (b) centered dark field image, zone axis close to $[01\bar{1}0]$, and (c) convergent beam diffraction pattern from the center of the SPP.

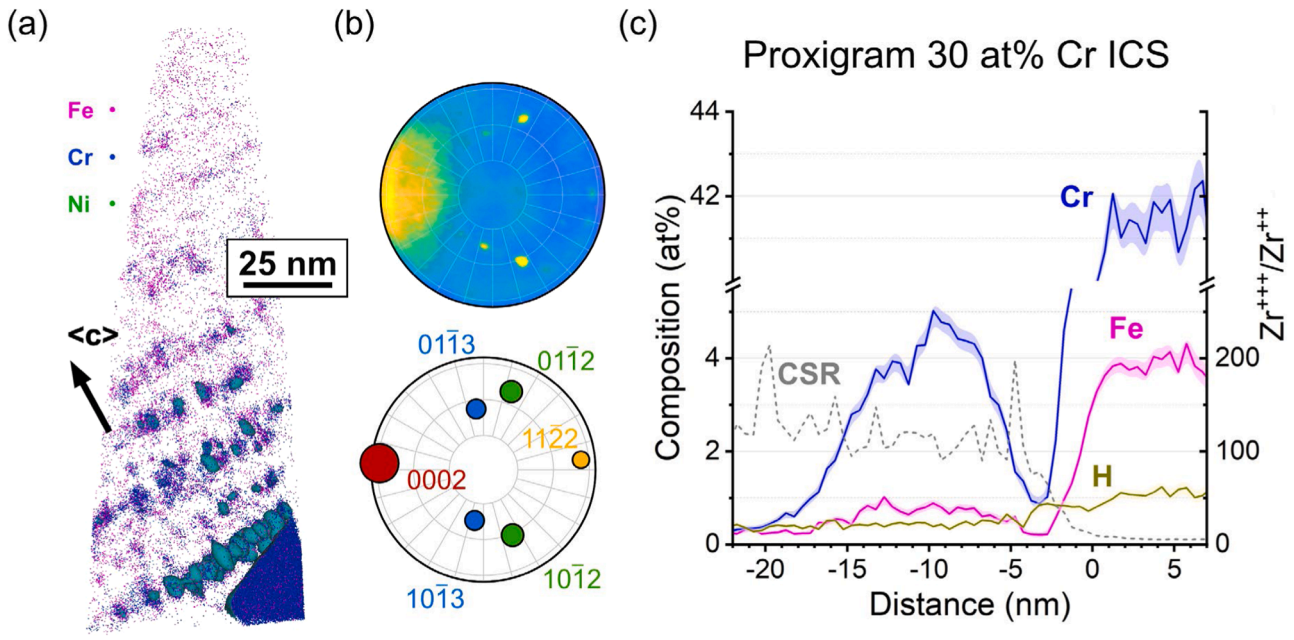

Fig. 2. Voltage pulsing APT measurement of a cryo-FIBed specimen capturing a dissolving Zr(Fe,Cr)$_2$-SPP and FeCr clusters in *Zircaloy-2 Fe+*. (a) Reconstruction displaying Fe, Cr, and (very few) Ni ions and a 30 at% Fe+Cr isoconcentration surface (ICS). (b) FEI and stereographic projection with identified poles. (c) Proximity histogram ('proxigram') of the 30 at% Cr ICS of the SPP. Experimental parameters: base temperature 92 K, 20% PF, 250 kHz pulse frequency, 0.2% target detection rate.

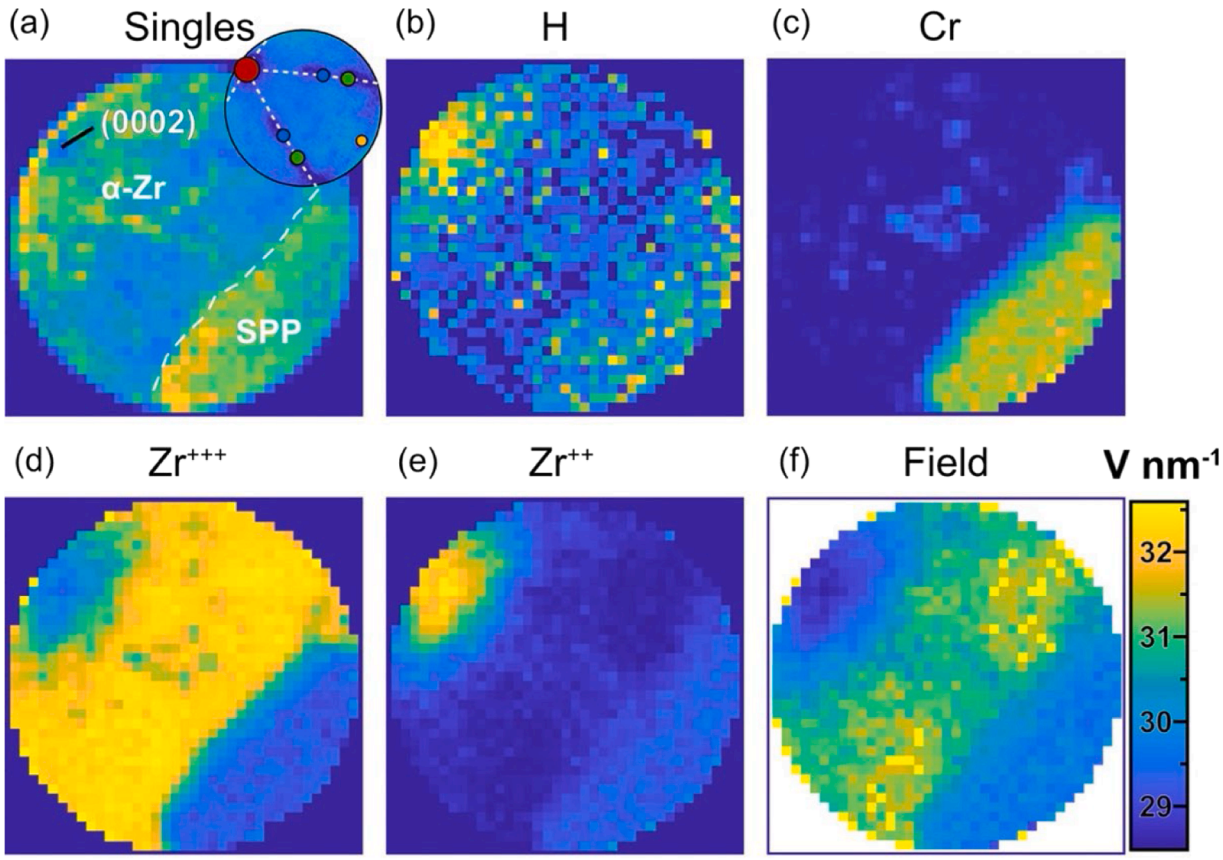

Fig. 3. Distribution of ionic and atomic species in the last 400,000 ions of the reconstruction in Fig. 2. (a) Single events showing high density in the SPP (lower right) and density variations in the α-Zr matrix, especially around the (0002) pole (see inset). (b) H map with increased H inside the SPP and around the (0002) pole. (c) is a Cr map. The three maps in (d)–(f) illustrate the changes in the evaporation field in terms of Zr: maps of (d) Zr^{+++}, (e) Zr^{++}and (f) the evaporation field calculated from the CSR according to [34].

the positions of further poles from the α-Zr matrix (similar to Fig. 2(b)). This pole is the position of highest fraction of H as shown in the map in Fig. 3(b). The SPP region, marked by the high Cr fraction in Fig. 3(c), shows a slightly increased H fraction in comparison to the α-Zr that is also reflected in the proxigram in Fig. 2(c), while it is slightly lower than at the (0002) pole. Fig. 3(c)–(f) provide information about the spatial distribution of the evaporation field. They show that there is a difference between the α-Zr matrix, the SPP, and the (0002) pole that is inversely correlated with the local H fractions. This is most evident from the maps showing the distribution of the Zr^{++} ions in (f) and the field strength in (e), which shows that the field is lowest at the (0002) pole (< 29 V/nm), highest in the α-Zr away from the main pole (up to 32 V/nm) and close to 30 V/nm inside the SPP. The apparent homogeneity of field and H distribution within the SPP might be related to the amorphous nature of the SPP, i.e., the absence of crystallographic planes.

Fig. 4(a) is a map of the atomic density of H (H^+ and ZrH^{++}ions) from a small APT data set (180,000 ions reconstructed, total 0.8 at% H) collected prior to the FIM experiment and a FIM image acquired at ~ 4944 V using Ne as imaging gas at a base temperature of 17 K. Black and white circles in Fig. 4(b) mark ideal pole positions inferred from a stereographic projection. We were not able to achieve stable imaging conditions, i.e., field ionization of Ne without evaporation from the specimen, which we cannot satisfactorily explain. It could be related to alloying elements of different evaporation fields present in the specimen – especially Sn with approximately 1.3 at%, which has a significantly lower evaporation field [33]. We calculated the global field based on the Zr ion charge states present in the mass to charge spectrum of the entire APT dataset. Since three charge states are found (Zr^{++}, Zr^{+++} and Zr^{++++}) we did the calculations for Zr^{+++}/Zr^{++} and Zr^{++++}/Zr^{+++}, which results in fields of ~ 30 and ~ 38 V/nm, respectively. The latter value has a rather high relative uncertainty of >20% due to the low number of quadruply charged ions [34] and was not considered for the following calculation. Using the value of ~ 30 V/nm for the field, we then estimated the apex radius at the end of the APT measurement, i.e., at the start of the FIM experiment (V_{end} = 4073 V, image compression factor = 1.36 from positions of crystallographic poles, k = 6.47 from adjustment of the interplanar spacings) to be r ~ 21 nm. This value appears to be reasonable since we have observed apex radii of FIB-sharpened specimens slightly larger than 10 nm by TEM (see Fig. S6). Using these values and the voltage at which we saw the best FIM image (~ 4944 V) we calculate a best imaging field (BIF) of ~ 36.4 V/nm, which is in good agreement with the value of 37 V/nm reported in [43]. It appears to be challenging to image Zr by FIM [44] and we did not find any report of imaging (0002) poles of hexagonal transition metals by FIM for comparison. It is however, not entirely clear why we did not observe formation of a stable FIM image, since it has been reported that even imaging of Al with He is possible at 20 K [45] and the evaporation field for Al is lower than that of Zr and the ionization field of He is higher than that of Ne. A potential but finally unsatisfactory explanation could be the presence of H, which is known to reduce the field necessary for ionization [46,47]. This however, is only expected at higher partial pressures of H_2 [47] and the global field we estimated is the typical one reported for Ne without addition of H_2, which also would have significantly altered the spectrum obtained in the APT experiment [41] prior to FIM. What can be more confidently explained is that terrasses away from the largely unidentifiable (0002) pole are clearer. This is likely caused by anisotropic evaporation resulting from the anisotropy of the work function [48,49], which is highest for (0002) planes [50]. The probability of an evaporation event is therefore highest around this pole leading to preferred removal of atoms, which then leads to a lower number of field ionization events per atom. In addition, the field is also lower due to the lower local curvature further reducing the number of field ionized Ne atoms.

The relevant difference of the specimen depicted in Fig. 5(a) (*Zircaloy-2,* 19 dpa) in comparison to the one from Figs. 2 and 3 is that annular milling was performed at RT, which caused significant H uptake leading to the expected transformation of the α-Zr matrix into δ-hydride [21–23]. This is demonstrated by the indexed FEI in (b) and also confirmed by the H profile in the proxigram in Fig. 5(c), which shows the large H fraction of the matrix. Like in the previously depicted case the H fraction shows an inverse relationship with the CSR: from the δ-hydride volume (measured H approximately 45 at%) the H fraction drops to below 10 at% (potentially even significantly lower, but the SPP volume is relatively small and at the edge of the dataset) while the CSR is low in the matrix and high inside the SPP. It is noteworthy that the field (~ 30 V/nm) inside the SPP is comparable to that found within the one in Fig. 2, while the field in the δ-hydride (former α-Zr) matrix (~ 28.5 V/nm) is much lower than in the α-Zr (~ 31.5 V/nm), which might be caused by the fact that the presence of H reduces the evaporation field of metals [46,51] or that the hydride has a lower density and the atoms are less strongly bonded. Note that the SPP volume captured is comparatively small but was the only voltage pulsing dataset of its kind that we obtained. H distributions in matrix and SPP as described above were also qualitatively observed in large Cr- and Fe-rich clusters, which resemble SPPs with respect to their composition but are more prone to APT related artifacts due to their smaller volumes.

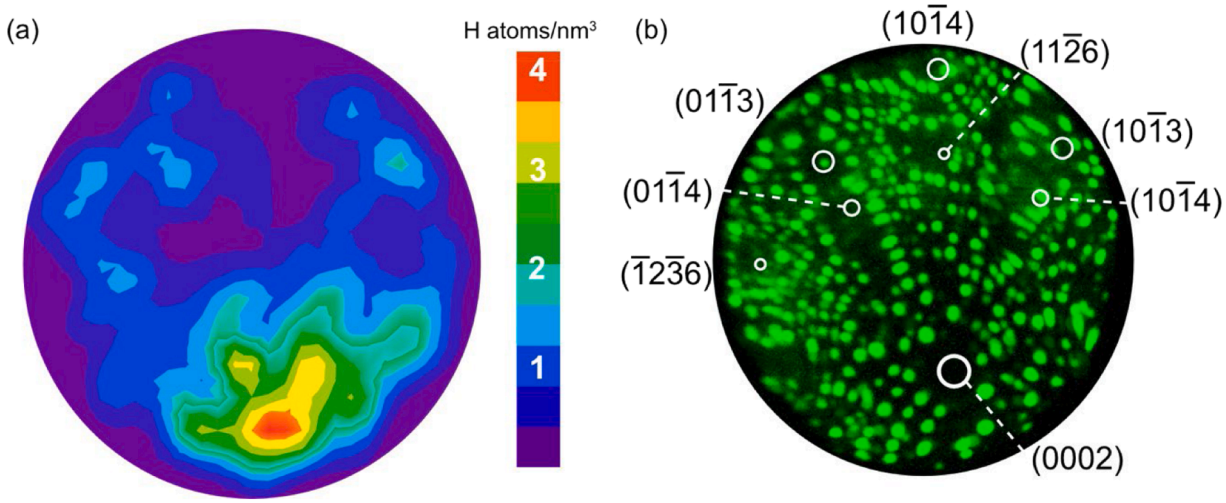

Fig. 4. Hydrogen distribution in α-Zr (*Zircaloy-2 Fe+*) around the (0002) pole. (a) 2D-map of the density of hydrogen (atoms/nm^3) from the APT dataset (around 180,000 ions) recorded before FIM imaging. (b) is an eFIM image taken at 17 K with pole positions from a stereographic projection overlay (white circles).

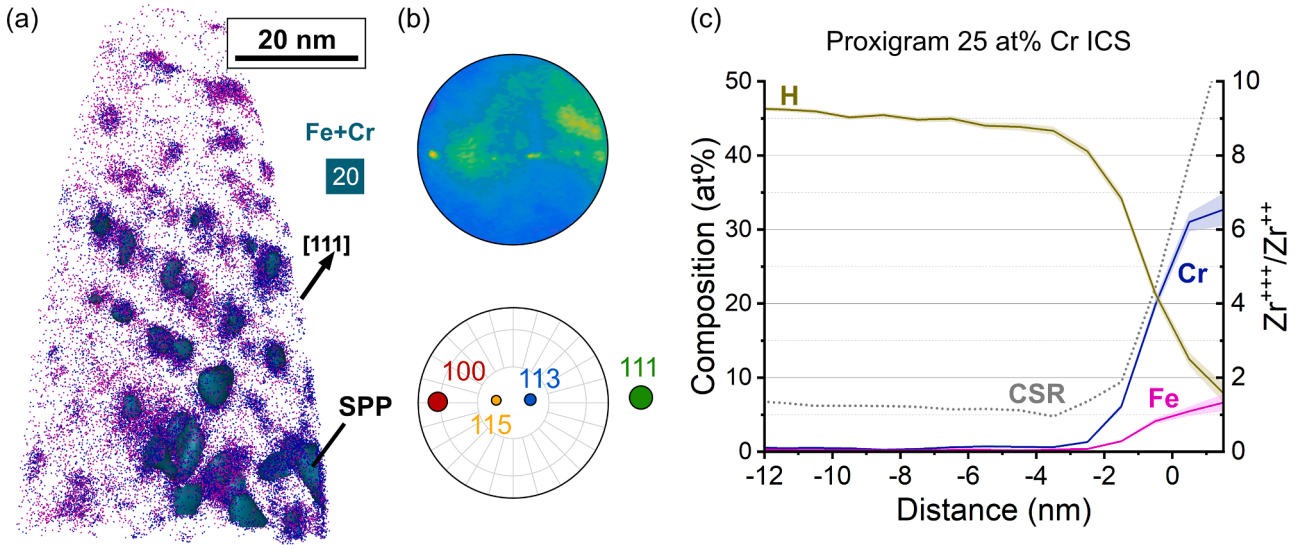

Fig. 5. Reconstruction from a voltage pulsing APT measurement of an RT-FIBed *Zircaloy-2* (19 dpa) specimen containing Cr-rich clusters including a small volume of a $Zr(Fe,Cr)_2$-SPP in Zircaloy-2. (a) Reconstruction displaying Fe and Cr ions and a 20 at% Fe+Cr ICS. (b) Proximity histogram of the 25 at% Cr ICS. Experimental parameters: base temperature 70 K, 20% PF, 200 kHz pulse frequency, 0.2% target detection rate.

3.3. Laser pulsing APT

Fig. 6 provides information from a laser pulsing measurement (LPE 60 pJ, 50 K, *Zircaloy-2,* 19 dpa) of a specimen sharpened under cryogenic conditions that captured a small fraction of a $Zr(Fe,Cr)_2$-SPP. Unfortunately, insights regarding the H distribution are very limited. The SPP is located at the apex of the specimen (see Fig. 6(a)) and has been partially oxidized during the transfer from the FIB instrument to the LEAP as can be seen in the ZrO ion map and the STEM image in (b). In other specimens that are not shown here we observed that in regions with significant O fractions, H was reduced and FIB-induced transformation into hydride was suppressed. We believe therefore that the measured H distribution in high O regions is not representative. In addition, the distribution of H-containing ionic species is strongly (anti) correlated with the laser incident side. This is illustrated in Fig. 6(c): the fractions of H^+ and H_2^+ are virtually zero on the side illuminated by the laser and unrealistically high on the opposite side. The ZrH^{++} fraction is close to zero at a similar position as well as at a crystallographic pole. Fig. 6(d) highlights a noteworthy observation, namely that the ZrH^{++} fraction – and not the H^+ and H_2^+ fractions – is reduced in Cr-clusters (dashed ellipses) compared to the matrix. Since they are located close to the center of the tip, these clusters are not oxidized and might indicate a lower affinity for hydrogen compared to the surrounding matrix. In this instance it is notable that the CSR is not changing significantly between the matrix and the clusters, which is depicted in the proxigram of one cluster in Fig. 6(e). To avoid incorporation of O-rich volumes in the calculation of the proxigram, a cylindrical volume with a 10 nm diameter near the center line of the specimen, i.e., away from the oxidized volume (see shaded area in (b)) was exported and the proxigram was then obtained from this sub-volume.

Fig. 7 is showcasing a section from a reconstruction of a dataset from a specimen FIB-milled at RT (LPE 50 pJ, 50 K, *Zircaloy-2,* 9 dpa) that contains a $Zr(Fe,Cr)_2$-SPP. Fig. 7(a) highlights the SPP and the Cr-rich clusters as well as Fe clusters, which are aligned parallel to a set of (111)-planes (δ-hydride). The maps in Fig. 7(b) show the atomic fractions of H, Cr and Fe from a 10 nm thick slice perpendicular to the specimen axis; the measured H fraction is inhomogeneously distributed and reaches unrealistically high values of up to 90 at%. In the SPP volume (high Cr and Fe) H is measured to be near 30 at%. The fraction of ZrH^{++} ions is close to zero inside the SPP (comparable to Fig. 6(d) and (e)) while $H^+$and H_2^+ are both detected there.

4. Discussion

4.1. FIB-based specimen preparation for H analysis by APT

It is well known that in order to perform meaningful H APT analyses of Zr and other metals that have high affinity to H, like Ti and Hf, annular milling by (both Ga and Xe-plasma) FIB [24] has to be performed at low temperatures that prevent the ingress of H into the material [23,24,52]. While investigating the 'real' H distribution therefore does not allow for RT-FIB preparation, samples prepared in that manner can still contain useful information. For example, they can be used as a simple way to experimentally assess the H affinity of a microstructure qualitatively (here SPPs, clusters, matrix). Furthermore, all other elements are not noticeably affected and analyses can be conducted irrespective of the H signal [23].

4.2. Pulsing mode and H detection

As a general statement, our results confirm what has been demonstrated in previous work on bulk Ti δ-hydride (TiD_2) [28] and FIB-induced Zr δ-hydride [23], namely that voltage pulsing is to be preferred when attempting H (or D) analysis. The main advantages are that overall, much less H is detected, fewer H-containing species (molecular ions) are found and the ionic density is more homogenous [28], i.e., there is for example no asymmetric distribution of H-containing species due to the laser illumination from one side as seen in Fig. 6 (see also [53]). Furthermore, laser pulsing of hydride specimens sometimes leads to very inhomogeneous H distributions, that do not resemble any known phases or microstructural features [28]; see Fig. 7 as a prime example where the H fraction varies between approximately 30 and 90 at% due to surface diffusion facilitated by heating through the laser [28]. However, in certain cases conclusions about H distributions can be obtained from laser pulsing APT, e.g., in cases where the H distribution cannot be explained by APT artefacts or acts in a manner opposed to the expected trend [53].

4.3. H distribution in SPPs and matrix

Table 3 provides a qualitative comparison of the APT measurements from different experimental work-flows: FIB-milling at ambient and cryogenic temperatures resulting either in transforming the specimen

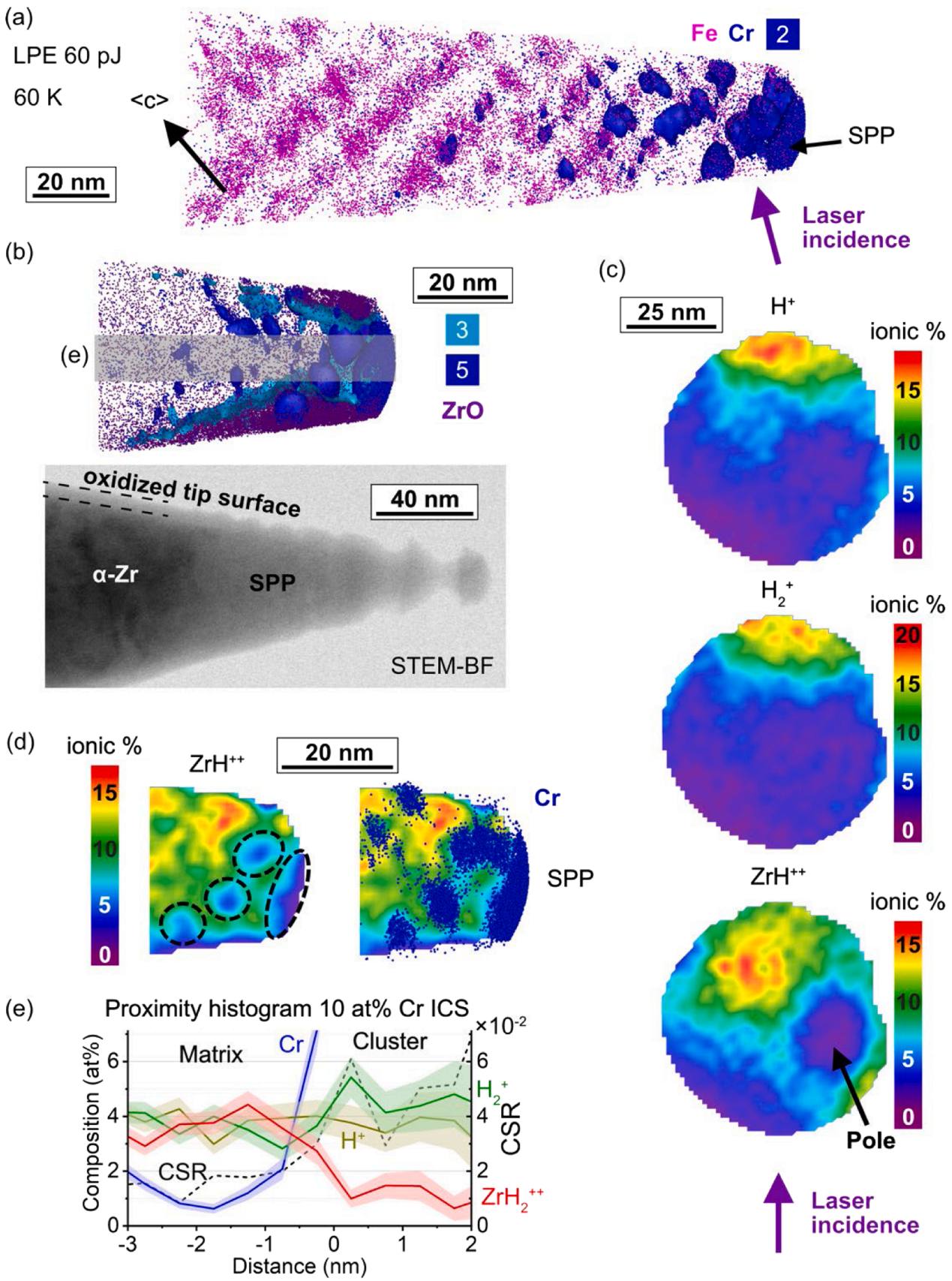

Fig. 6. Laser pulsing dataset of a cryo-FIBed specimen from Zircaloy-2 cladding tube with a $Zr(Fe,Cr)_2$-SPP at the apex: (a) Fe clusters and some FeCr clusters arranged in layers on basal planes. (b) 10 nm slice with ZrO ions, and O and Cr ICSs, and a STEM micrograph. (c) H^+, H_2^+ and ZrH^{++} maps from a 5 nm slice. (d) ZrH^{++} map of the apex from a 5 nm slice with and without the Cr ions in the volume. (e) Proxigram of a Cr-rich cluster, including the Zr^{+++}/Zr^{++} CSR curve. Experimental parameters: base temperature 60 K, 50 pJ LPE, 200 kHz pulse frequency, 0.5% target detection rate.

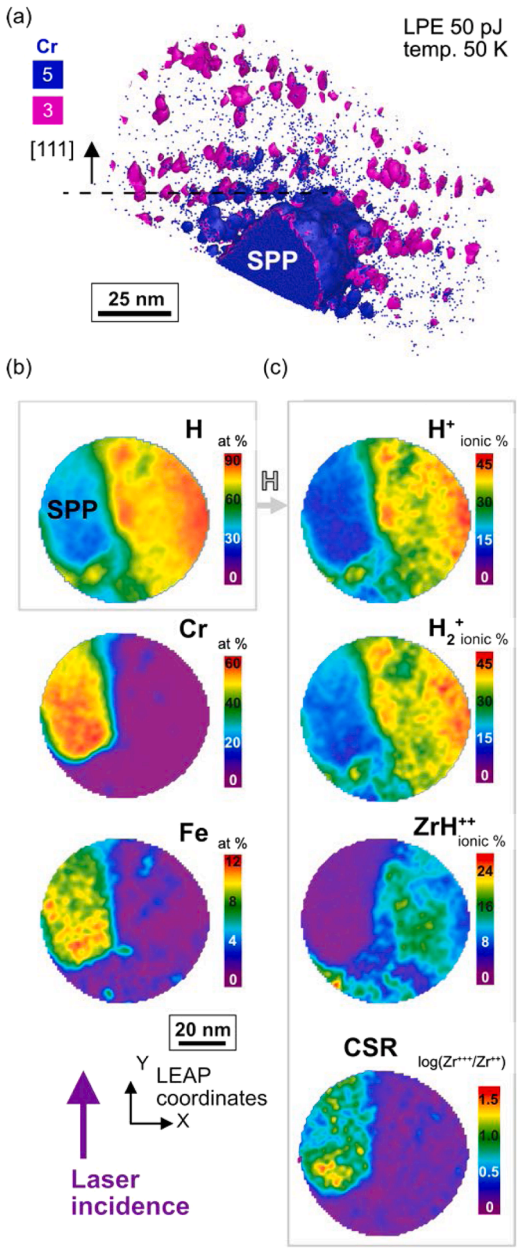

Fig. 7. Laser pulsing dataset of an RT-FIBed specimen from *Zircaloy-2* cladding tube (9 dpa). (a) highlights the SPP and the Cr- and Fe-rich clusters with the layers edge-on. (b) Composition maps of H, Cr and Fe. (c) Maps showing the ionic fractions of H^+, H_2^+ and ZrH^{++} and the CSR. Experimental parameters: base temperature 50 K, 50 pJ LPE, 100 and 200 kHz pulse frequency, 0.5% target detection rate.

Table 3
Qualitative overview of H fractions in different APT experiments.

Phase	Pulsing mode	Relative CSR/ field in the SPP with respect to matrix	H fraction in SPP compared to matrix	Figure
α-Zr	Voltage	low (~ 30 V/nm similar to SPP in δ-hydride)	high	2–4
	Laser	high	low, cluster used as proxy	6
δ-hydride	Voltage	high (~ 30 V/nm similar to SPP in α-Zr)	low	5
	Laser	high	low	7

into δ-hydride or in preserving α-Zr followed by APT in voltage and laser pulsing modes. The table lists the relative field strengths ('high' and 'low') inside the SPPs with respect to the surrounding phase, α-Zr or δ-hydride, and the locations of relatively higher measured H fraction.

The bulk H concentration of the parent sample of our specimen most suitable for H analysis (cryo-FIB and voltage pulsing, see Figs. 2 and 3) from the *Zircaloy-2 Fe+* tube was ~ 1.2 at%. The vast majority of this H is bound in (δ) hydrides and the solubility of H in α-Zr is not higher than some ppm at RT [54]. The significantly larger fraction of detected H during the APT experiment inside the α-Zr matrix therefore needs to be explained. We attribute this to contaminant H_2 as main source that is adsorbed onto the specimen surface [47] or may be field ionized [55], likely to a smaller extent [20]. As the amount of contaminant H in APT under otherwise unaltered conditions depends approximately linearly on the time between pulses [56–58], we varied the pulse frequency in measuring δ-hydrides to assess the fraction of H from this source. From this measurement it could be concluded that in voltage pulsing measurements at a pulse frequency of 200 kHz the contaminant H fraction should be somewhat below 1 at% [23]. Assuming that the effect is similar for α-Zr and the total detected H fractions in the datasets shown in Figs. 2 and 3 are ~ 0.8 at% and ~ 1.0 at%, respectively, these are hence most likely to a large extent contaminant H and in addition the low detection rate of 0.2% is likely to increase the amount of adsorbed H [56]. The measured local H fractions are related to differences in surface field magnitude. We found that the measured detection of 'H enrichment' in the $Zr(Fe,Cr)_2$-SPP in Fig. 2 is correlated with a lower field (see Fig. 3). The correlation of local field magnitude and H fraction is also shown in α-Zr away from SPPs as seen in Figs. 3 and 4. At first glance a simple inverse relationship of field strength and H fraction as seen in Fig. 3(d)–(f) appears to be an intriguing explanation, but it is likely too simplistic, as the opposite trend would expected from reports in the literature [60,61].

One can readily assume that H is highly mobile on the specimen surface, especially in rather high temperature conditions that our experiments were conducted at [59] (to put this into perspective, solute C and N are mobile across many tens of nm at 40 K [38]). Such surface migration along zone lines explains the manner in how it reaches preferential evaporation sites. This also means that the initial location of most H atoms will be obscured no matter if originating from contaminant H_2 or from within the specimen.

The magnitude of the local field is related to the local curvature, the crystallographic direction and the chemical identity of the atoms present there. The adsorption and the magnitude of coverage are DC field-dependent (i.e., the pulse fraction plays a role) and there appears to be a DC field range in which there is a local maximum in adsorption and hence detected H around 35 V/nm [60,61]. Adsorption is also taking place differently on different crystallographic planes [58,59]. In addition, desorption of H/H_2 is field dependent, with 'low' fields leading to H_2^+ formation and 'high' fields leading to H^+.

Based on what has been reported in the literature, one would expect that H migration takes place leading to evaporation at high-field poles. What is observed (see Figs. 3 and 4) instead, is that, while H is preferentially found at the (0002) pole this is a low- rather than a high-field region. We can attribute this lower field at the (0002) pole to the lower evaporation field (due to the larger work function, see 3.2), that results in a 'flattening' of the tip around this pole and hence lower curvature that causes a lower field enhancement. An explanation for the preferred evaporation from this pole (and to a lesser extent the SPP region) could be a potential increase in coverage of these surfaces as binding energies of H/H_2 vary widely [20]. In conclusion we have to state that we were not able to produce reliable evidence for the trapping of H close to or at SPPs.

The results from the voltage pulsing measurement shown in Fig. 5 provide evidence for the higher affinity of Zr for H compared to the Zr $(Fe,Cr)_2$-SPP since the FIB-induced H ingress led to the expected α-Zr → δ-hydride formation of the matrix but the SPP did not transform or take

up H, the same interpretation is in principle valid for Fig. 7. DFT simulations of $Zr(Cr)_2$ [62] and $Zr(Fe,Cr)_2$ [5] in Zircaloy-2 have shown a higher affinity of the Zr matrix for H than these intermetallics. Based on these results it seems reasonable to propose that the same is likely the case for the irradiated SPPs presented here. It should be pointed out that irradiated $Zr(Fe,Cr)_2$-SPPs are amorphous and hence the nature of the interfaces with the α-Zr matrix differs from that with initially crystalline precipitates. Therefore, (tensile) strains due to thermal mismatches that might have been present initially, and are supposedly contributing to H affinity of the interface region, possibly disappear during irradiation and might not constitute H traps any longer. The measured SPP composition here is close to Zr_1:$(Cr,Fe)_1$ – due to preferential release of Fe into the matrix – only a small fraction of Fe is left (e.g., 4 at% Fe vs. 42 at% Cr for the SPP shown in Fig. 2). In light of the complications introduced by laser pulsing, the assessment of samples without D charging can be only qualitative at best, but can still provide useful information in a few select cases [53].

4.4. Relevance of APT H analysis on (irradiated) Zr

In the work presented above we tried to obtain information from 'real' material that has several limitations with respect to the experimental options.

- Due to the cladding tubes being radioactive many experimental options that require handling of macroscopic samples cannot be pursued. We were therefore limited to experimental techniques that are accessible to physically small specimens lifted out from the sectioned tubes by FIB.
- The cladding tube samples that we extracted APT specimens from had spent roughly 10 years cooling down post operation, which makes any conclusions about the status during operation speculative.
- It is likely that a significant fraction of the hydrides present in the cold tubes precipitated upon cooling from supersaturated α-Zr (maximum H solubility at 300 °C is around 1 at% [54]) and it is very unlikely that diffusible hydrogen is still present after cooling.

Despite these limitations, we can draw some conclusions that might benefit further investigations:

- In agreement with the known high affinity of Zr for H, we observed that FIB-induced hydride formation of the α-Zr matrix known to occur does not take place in SPPs. This indicates that they have a lower H affinity not only as intact crystals [5] but also in their amorphous state, which has so far not been assessed by simulations.
- Jones et al. [5] performed their SIMS measurements more than half a year after the autoclave experiment with D_2O had been conducted and still found D concentrated close to SPPs. Drawing furthermore on DFT modelling this was considered evidence of strong trapping around some SPPs. Based on these observations it appears to be possible – even likely – that such trapping also takes place in the materials that we investigated. However, we could not confirm that H trapping occurs in the case of our specimens, rather we have shown that the local H fraction appears to be connected to the magnitude of the field. It is also highly likely that the detected H is originating from contaminant H_2. Even if a small fraction of the H detected is indeed originating from the material there is no way of identifying it and hence the experimental procedure that we employed is not sufficient to assess trapping of H in α-Zr by APT.

4.5. Proposed workflow for APT H analysis on irradiated Zr

Since Zr has a high affinity to H it is not possible to avoid all ways of H contamination during preparation and experiment [20]. An ideal experiment would entail cryogenic FIB preparation of specimens from reactor-irradiated material using a Xe-beam (to minimize FIB-induced irradiation damage [63]) followed by D gas charging [64,65] (the success of this step is not certain since some elevation in temperature is needed but it should not lead to deuteride formation) and quenching, which would freeze D that is located in positions where it is not strongly bonded. This would then be followed by *voltage* pulsing atom probe (resulting usually in very small datasets before specimen fracture) ideally in an APT instrument where the analysis chamber is manufactured from Ti, resulting in a very low H background [19]. In addition, the pulse frequency should be changed during the measurement to potentially assess, which fraction of H (and D) that is originating from inside the specimen [56]. While all of this can be done in principle, there exists to our knowledge currently no single laboratory combining all the equipment listed above. In addition, limited availability of (neutron) irradiated samples and restrictions in transport and handling, the low survivability of α-Zr in voltage APT, and the low probability of capturing an SPP, make such an endeavor challenging to say the least. Alternatively, neutron (or proton) irradiated bulk samples can be charged with D in spiked water, either electrochemically or by further autoclave corrosion. Standard lift-out and sharpening by (cryo) FIB and APT could then be carried out at specific regions in which D is proposed to be strongly bonded. An elegant approach would be to conduct analysis on Zircaloy components from operation in CANDU reactors where heavy water is used as moderator and coolant and hence HPU includes D. This approach might be less relevant with respect to the specific questions relevant for Zircaloy fuel cladding since pressure tubes (the equivalent to fuel cladding in most other water-moderated reactor types) have been manufactured from Zr-2.5Nb for decades [66], and hence do not contain Fe- and Cr-rich SPPs. Still, for understanding of fundamentals of H (and D) behavior in Zr alloys this might well be worth trying.

5. Conclusions

We have performed in-depth analyses of H in APT data of $Zr(Fe,Cr)_2$-SPPs from Zircaloy-2-type fuel cladding subjected to 2082 days of reactor operation. As was expected from previous work, the feasibility of such analysis depends strongly on preparation workflows and the experimental parameters of the APT experiments. The main insights from this study are:

- The amorphous SPPs are significantly less accommodating for H than the α-Zr matrix. This has been demonstrated by RT-FIB preparation, which led to transformation of the α-Zr matrix into δ-hydride while the SPPs did not exhibit such massive H uptake. This tendency is in agreement with experimental and modelling evidence for crystalline SPPs without irradiation.
- In agreement with the literature, laser pulsing APT should be avoided whenever possible. Even on cryo-FIB-sharpened specimens that do not see massive H ingress, the H distribution (main H supply is the contaminant H_2 from the vacuum chamber) is strongly correlated with the laser incident direction.
- Even optimized workflows, i.e., cryo-FIB specimen sharpening followed by voltage pulsing APT, do not alleviate the limitations in commercial instruments with contaminant H_2. Distinguishing between H originating from the specimen vs. that from the chamber is not possible.
- We demonstrated that the apparent H distribution (i.e., enrichment inside an SPP situated in an α-Zr matrix) is associated with the local field strength, which in turn is depending on local composition and more significantly on the crystallography. The most promising – and very challenging – way to assess the 'real' H distribution in and around SPPs by APT is likely deuterium (or tritium) gas-charging of cryo-FIBed specimens.

CRediT authorship contribution statement

David Mayweg: Writing – review & editing, Writing – original draft,

Visualization, Investigation, Formal analysis, Data curation, Conceptualization. **Johan Eriksson:** Writing – review & editing, Investigation, Formal analysis, Conceptualization. **Mohammad Sattari:** Writing – review & editing, Investigation. **Mattias Thuvander:** Writing – review & editing, Supervision, Investigation, Funding acquisition.

Declaration of competing interest

The authors declare that they have no known competing financial interests or personal relationships that could have appeared to influence the work reported in this paper.

Data availability

Data will be made available on request.

Acknowledgements

DM is thankful for funding from the *Swedish Centre for Nuclear Technology* (SKC). This work received funding from *Westinghouse Electric Sweden AB, OKG AB, Vattenfall AB* and *EPRI*. We thank Hans-Olof Andrén and Gustav Sundell for fruitful discussions. Pia Tejland (*Studsvik Nuclear AB*) and Magnus Limbäck (*Westinghouse Electric Sweden AB*) are acknowledged for providing the cladding tube samples. Atom probe experiments were carried out at Chalmers Materials Analysis Laboratory (CMAL). DM wants to extend thanks to Baptiste Gault for helpful comments on H analysis by APT and interpretation of FIM images and Levi Tegg for support in assessment of the calculations of the field strengths using CSRs.

Supplementary materials

Supplementary material associated with this article can be found, in the online version, at doi:10.1016/j.jnucmat.2024.155343.

References

[1] C.E. Ells, Hydride precipitates in zirconium alloys (A review), J. Nucl. Mater. 28 (2) (1968) 129–151.
[2] J. Eriksson, D. Mayweg, G. Sundell, H.O. Andrén, M. Thuvander, Solute concentrations in the matrix of zirconium alloys studied by atom probe tomography, in: S.K. Yagnik, M. Preuss (Eds.) ASTM STP 1645, Ottawa, 2023, pp. 149–172.
[3] P. Chemelle, D.B. Knorr, J.B. Van Der Sande, R.M. Pelloux, Morphology and composition of second phase particles in zircaloy-2, J. Nucl. Mater. 113 (1) (1983) 58–64.
[4] P.A. Burr, S.T. Murphy, S.C. Lumley, M.R. Wenman, R.W. Grimes, Hydrogen solubility in zirconium intermetallic second phase particles, J. Nucl. Mater. 443 (1–3) (2013) 502–506.
[5] C. Jones, V. Tuli, Z. Shah, M. Gass, P.A. Burr, M. Preuss, K.L. Moore, Evidence of hydrogen trapping at second phase particles in zirconium alloys, Sci. Rep. 11 (1) (2021) 4370.
[6] Z. Shah, Characterizing and Modelling Precipitation in Zirconium Alloys, University of Manchester, 2019.
[7] W.J.S. Yang, R.P. Tucker, B. Cheng, R.B. Adamson, Precipitates in zircaloy: identification and the effects of irradiation and thermal treatment, J. Nucl. Mater. 138 (2) (1986) 185–195.
[8] G. Sundell, M. Thuvander, P. Tejland, M. Dahlbäck, L. Hallstadius, H.-O. Andrén, Redistribution of alloying elements in Zircaloy-2 after in-reactor exposure, J. Nucl. Mater. 454 (1–3) (2014) 178–185.
[9] A. Harte, D. Jädernäs, M. Topping, P. Frankel, C.P. Race, J. Romero, L. Hallstadius, E.C. Darby, M. Preuss, The effect of matrix chemistry on dislocation evolution in an irradiated Zr alloy, Acta Mater. 130 (2017) 69–82.
[10] T. Sawabe, T. Sonoda, Evolution of nanoscopic iron clusters in irradiated zirconium alloys with different iron contents, J. Nucl. Sci. Technol. 55 (10) (2018) 1110–1118.
[11] G.J.C. Carpenter, D.O. Northwood, The contribution of dislocation loops to radiation growth and creep of Zircaloy-2, J. Nucl. Mater. 56 (1975) 260–266.
[12] D.O. Northwood, R.W. Gilbert, L.E. Bahen, P.M. Kelly, R.G. Blake, A. Jostsons, P. K. Madden, D. Faulkner, W. Bell, R.B. Adamson, Characterization of neutron irradiation damage in zirconium alloys–an international "round-robin" experiment, J. Nucl. Mater. 79 (2) (1979) 379–394.
[13] B. Gault, A. Chiaramonti, O. Cojocaru-Mirédin, P. Stender, R. Dubosq, C. Freysoldt, S.K. Makineni, T. Li, M. Moody, J.M. Cairney, Atom probe tomography, Nat. Rev. Methods Primers 1 (1) (2021) 51.
[14] T.T. Tsong, T.J. Kinkus, C.F. Ai, Field induced and surface catalyzed formation of novel ions: a pulsed-laser time-of-flight atom-probe study, J. Chem. Phys. 78 (7) (1983) 4763–4775.
[15] J. Takahashi, K. Kawakami, Y. Kobayashi, T. Tarui, The first direct observation of hydrogen trapping sites in TiC precipitation-hardening steel through atom probe tomography, Scr. Mater. 63 (2010) 261–264.
[16] B. Gault, A. Saksena, X. Sauvage, P. Bagot, L.S. Aota, J. Arlt, L.T. Belkacemi, T. Boll, Y.S. Chen, L. Daly, M.B. Djukic, J.O. Douglas, M.J. Duarte, P.J. Felfer, R.G. Forbes, J. Fu, H.M. Gardner, R. Gemma, S.S.A. Gerstl, Y.A. Gong, G. Hachet, S.A. Jakob, B. M. Jenkins, M.E. Jones, H. Khanchandani, P. Kontis, M. Krämer, M. Kühbach, R.K. W. Marceau, D. Mayweg, K.L. Moore, V. Nallathambi, B.C. Ott, J.D. Poplawsky, T. Prosa, A. Pundt, M. Saha, T.M. Schwarz, Y. Shang, X. Shen, M. Vrellou, Y. Yu, Y. Zhao, H. Zhao, B. Zou, Towards establishing best practice in the analysis of hydrogen and deuterium by atom probe tomography, Microsc. Microanal. (2024) accepted manuscript.
[17] I. Mouton, A.J. Breen, S. Wang, Y. Chang, A. Szczepaniak, P. Kontis, L. T. Stephenson, D. Raabe, M. Herbig, T.B. Britton, B. Gault, Quantification challenges for atom probe tomography of hydrogen and deuterium in zircaloy-4, Microsc. Microanal. 25 (2) (2019) 481–488.
[18] M.E. Jones, A.J. London, A.J. Breen, P.D. Styman, S. Sikotra, M.P. Moody, D. Haley, Improving the quantification of deuterium in zirconium alloy atom probe tomography data using existing analysis methods, Microsc. Microanal. 28 (4) (2021) 1245–1254.
[19] P. Felfer, B. Ott, M. Monajem, V. Dalbauer, M. Heller, J. Josten, C. Macaulay, An atom probe with ultra-low hydrogen background, Microsc. Microanal. 28 (4) (2022) 1255–1263.
[20] S.H. Yoo, S.H. Kim, E. Woods, B. Gault, M. Todorova, J. Neugebauer, Origins of the hydrogen signal in atom probe tomography: case studies of alkali and noble metals, New J. Phys. 24 (1) (2022) 013008.
[21] S.M. Hanlon, S.Y. Persaud, F. Long, A. Korinek, M.R. Daymond, A solution to FIB induced artefact hydrides in Zr alloys, J. Nucl. Mater. 515 (2019) 122–134.
[22] I. Mouton, Y. Chang, P. Chakraborty, S. Wang, L.T. Stephenson, T. Ben Britton, B. Gault, Hydride growth mechanism in zircaloy-4: investigation of the partitioning of alloying elements, Materialia 15 (2021) 101006.
[23] D. Mayweg, J. Eriksson, O. Bäcke, A.J. Breen, M. Thuvander, Focused ion beam induced hydride formation does not affect Fe, Ni, Cr-clusters in irradiated Zircaloy-2, J. Nucl. Mater. 581 (2023) 154444.
[24] Y. Chang, W. Lu, J. Guenole, L.T. Stephenson, A. Szczpaniak, P. Kontis, A. K. Ackerman, F.F. Dear, I. Mouton, X. Zhong, S. Zhang, D. Dye, C.H. Liebscher, D. Ponge, S. Korte-Kerzel, D. Raabe, B. Gault, Ti and its alloys as examples of cryogenic focused ion beam milling of environmentally-sensitive materials, Nat. Commun. 10 (1) (2019) 942.
[25] D. Mayweg, J. Eriksson, M. Sattari, G. Sundell, M. Limbäck, I. Panas, H.-O. Andrén, M. Thuvander, Formation of pure zirconium islands inside c-component loops in high-burnup fuel cladding, J. Nucl. Mater. (2024) 155116.
[26] K. Kakiuchi, N. Itagaki, T. Furuya, A. Miyazaki, Y. Ishii, S. Suzuki, T. Terai, M. Yamawaki, Effect of iron on hydrogen absorption properties of zirconium alloys, J. Phys. Chem. Solids 66 (2) (2005) 308–311.
[27] K. Thompson, D. Lawrence, D.J. Larson, J.D. Olson, T.F. Kelly, B. Gorman, *In situ* site-specific specimen preparation for atom probe tomography, Ultramicroscopy 107 (2–3) (2007) 131–139.
[28] Y.H. Chang, I. Mouton, L. Stephenson, M. Ashton, G.K. Zhang, A. Szczpaniak, W. J. Lu, D. Ponge, D. Raabe, B. Gault, Quantification of solute deuterium in titanium deuteride by atom probe tomography with both laser pulsing and high-voltage pulsing: influence of the surface electric field, New J. Phys. 21 (5) (2019) 053025.
[29] B. Gault, D. Haley, F. de Geuser, M.P. Moody, E.A. Marquis, D.J. Larson, B. P. Geiser, Advances in the reconstruction of atom probe tomography data, Ultramicroscopy 111 (6) (2011) 448–457.
[30] B. Gault, F. de Geuser, L.T. Stephenson, M.P. Moody, B.C. Muddle, S.P. Ringer, Estimation of the reconstruction parameters for atom probe tomography, Microsc. Microanal. 14 (4) (2008) 296–305.
[31] A.J. Breen, A.C. Day, B. Lim, W.J. Davids, S.P. Ringer, Revealing latent pole and zone line information in atom probe detector maps using crystallographically correlated metrics, Ultramicroscopy 243 (2023) 113640.
[32] M. Heller, B. Ott, V. Dalbauer, P. Felfer, A MATLAB toolbox for findable, accessible, interoperable, and reusable atom probe data science, Microsc. Microanal. (2024).
[33] D.R. Kingham, The post-ionization of field evaporated ions: a theoretical explanation of multiple charge states, Surf. Sci. 116 (2) (1982) 273–301.
[34] L. Tegg, L.T. Stephenson, J.M. Cairney, Estimation of the electric field in atom probe tomography experiments using charge state ratios, Microsc. Microanal. 30 (3) (2024) 466–475..
[35] J. Eriksson, G. Sundell, P. Tejland, H.-O. Andrén, M. Thuvander, Nanoscale chemistry of Zircaloy-2 exposed to three and nine annual cycles of boiling water reactor operation–an atom probe tomography study, J. Nucl. Mater. 561 (2022) 153537.
[36] Y. Takagawa, S. Ishimoto, Y. Etoh, T. Kubo, K. Ogata, O. Kubota, The correlation between microstructures and in-BWR corrosion behavior of highly irradiated Zr-based alloys, J. ASTM Int. 2 (1) (2005) JAI12357.
[37] T.T. Tsong, G. Kellogg, Direct observation of the directional walk of single adatoms and the adatom polarizability, Phys. Rev. B 12 (4) (1975) 1343–1353.
[38] B. Gault, F. Danoix, K. Hoummada, D. Mangelinck, H. Leitner, Impact of directional walk on atom probe microanalysis, Ultramicroscopy 113 (2012) 182–191.

[39] M.G. Inghram, R. Gomer, Mass Spectrometric Analysis of Ions from the Field Microscope, J. Chem. Phys. 22 (7) (1954) 1279–1280.
[40] T.C. Clements, E.W. Müller, Occurrence of H3+ in the field ionization of hydrogen, J. Chem. Phys. 37 (11) (1962) 2684–2687.
[41] S.V. Krishnaswamy, E.W. Müller, Metal hydrides in pulsed field evaporation, Z. Phys. Chem. 104 (1–3) (1977) 121–130.
[42] O.C. Hellman, J.A. Vandenbroucke, J. Rüsing, D. Isheim, D.N. Seidman, Analysis of three-dimensional atom-probe data by the proximity histogram, Microsc. Microanal. 6 (5) (2000) 437–444.
[43] K. Hono, S.S. Babu, Atom-probe field ion microscopy, (2014) 1453–1589.
[44] J.J. Carroll, A.J. Melmed, Field ion microscopy of zirconium, Surf. Sci. 58 (2) (1976) 601–604.
[45] T. Abe, K. Miyazaki, K.I. Hirano, Imaging of pure Al and aged Al-4wt%Cu alloys by field-ion microscope, Acta Metall. 30 (2) (1982) 357–366.
[46] E.W. Müller, S. Nakamura, O. Nishikawa, S.B. McLane, Gas-surface interactions and field-ion microscopy of nonrefractory metals, J. Appl. Phys. 36 (8) (1965) 2496–2503.
[47] E.W. Müller, Hydrogen promotion of field ionization and rearrangement of surface charge, Surf. Sci. 7 (3) (1967) 462–473.
[48] D.G. Brandon, The resolution of atomic structure: recent advances in the theory and development of the field ion microscope, Br. J. Appl. Phys. 14 (8) (1963) 474.
[49] R.G. Forbes, New activation-energy formulae for charge-exchange type mechanisms of field evaporation, Surf. Sci. 116 (2) (1982) L195–L201.
[50] H. Kawano, Effective work functions of the elements, Prog. Surf. Sci. 97 (1) (2022).
[51] M. Wada, R. Uemori, O. Nishikawa, Effect of hydrogen on the evaporation field of metals, Surf. Sci. 134 (1) (1983) 17–29.
[52] R. Thomas, D. Lunt, M.D. Atkinson, J. Quinta da Fonseca, M. Preuss, F. Barton, J. O'Hanlon, P. Frankel, Characterisation of irradiation enhanced strain localisation in a zirconium alloy, Materialia 5 (2019).
[53] B.M. Jenkins, J. Haley, L. Chen, B. Gault, P.A. Burr, A. Callow, M.P. Moody, C.R. M. Grovenor, Experimental and modelling evidence for hydrogen trapping at a β-Nb second phase particle and Nb-rich nanoclusters in neutron-irradiated low Sn ZIRLO, J. Nucl. Mater. 587 (2023) 154755.
[54] E. Zuzek, J.P. Abriata, A. San-Martin, F.D. Manchester, The H-Zr (hydrogen-zirconium) system, Bull. Alloy Phase Diagr. 11 (4) (1990) 385–395.
[55] R.G. Forbes, Field-ion imaging old and new, Appl. Surf. Sci. 94-95 (1996) 1–16.
[56] M.S. Meier, M.E. Jones, P.J. Felfer, M.P. Moody, D. Haley, Extending estimating hydrogen content in atom probe tomography experiments where H2 molecule formation occurs, Microsc. Microanal. 28 (4) (2021) 1231–1244.
[57] G.L. Kellogg, Pulsed laser stimulated field desorption of hydrogen from molybdenum, J. Chem. Phys. 74 (2) (1981) 1479–1487.
[58] G. Sundell, M. Thuvander, H.-O. Andrén, Hydrogen analysis in APT: methods to control adsorption and dissociation of H2, Ultramicroscopy 132 (2013) 285–289.
[59] M. Martinka, Surface distributions of hydrogen field adsorbed on rhodium as displayed by imaging atom-probe, Surf. Sci. 109 (3) (1981) L539–L544.
[60] H.-O. Andrén, U. Rolander, Field dependence of hydrogen adsorption, Surf. Sci. 266 (1) (1992) 76–80.
[61] M. Hellsing, B. Hellsing, Field adsorption and desorption of hydrogen on W(110)–an atom-probe study, Surf. Sci. 176 (1) (1986) 249–260.
[62] P.A. Burr, S.T. Murphy, S.C. Lumley, M.R. Wenman, R.W. Grimes, Hydrogen accommodation in Zr second phase particles: implications for H pick-up and hydriding of Zircaloy-2 and Zircaloy-4, Corros. Sci. 69 (2013) 1–4.
[63] A. Saksena, B. Sun, X. Dong, H. Khanchandani, D. Ponge, B. Gault, Optimizing site-specific specimen preparation for atom probe tomography by using hydrogen for visualizing radiation-induced damage, Int. J. Hydrog. Energy (2023).
[64] A.A. El-Zoka, L.T. Stephenson, S.H. Kim, B. Gault, D. Raabe, The fate of water in hydrogen-based iron oxide reduction, Adv. Sci. 10 (24) (2023) e2300626 (Weinh).
[65] H. Khanchandani, A.A. El-Zoka, S.H. Kim, U. Tezins, D. Vogel, A. Sturm, D. Raabe, B. Gault, L.T. Stephenson, Laser-equipped gas reaction chamber for probing environmentally sensitive materials at near atomic scale, PLoS ONE 17 (2) (2022) e0262543.
[66] A. Sawatzky, C.E. Ells, Understanding Hydrogen in Zirconium, in: G.P. Sabol, G.D. Moan (Eds.), in: Proceedings of the Zirconium in the Nuclear Industry: Twelfth International Symposium ASTM STP 1354, West Conshohocken, PA, ASTM International, 2000, pp. 32–48.